A functional structural model of grass development based on metabolic regulation and coordination rules

Marion Gauthier, Romain Barillot, Anne Schneider, Camille Chambon, Christian Fournier, Christophe Pradal, Corinne Robert, Bruno Andrieu

Journal of Experimental Botany
doi:10.1093/jxb/eraa276 Advance Access Publication 4 June 2020

RESEARCH PAPER

A functional structural model of grass development based on metabolic regulation and coordination rules

Marion Gauthier[1,2,†], Romain Barillot[3,*,†], Anne Schneider[4], Camille Chambon[1], Christian Fournier[5], Christophe Pradal[6,7], Corinne Robert[1], and Bruno Andrieu[1]

[1] Université Paris-Saclay, INRAE, AgroParisTech, UMR ECOSYS, F-78850 Thiverval-Grignon, France
[2] ITK, Avenue de l'Europe, F-34830 Clapiers, France
[3] INRAE, UR P3F, F-86600 Lusignan, France
[4] Université d'Angers, INRAE, Agrocampus-Ouest, SFR 4207 QUASAV, IRHS, F-49071 Angers, France
[5] Université de Montpellier, INRAE, Montpellier SupAgro, UMR LEPSE, F-34060 Montpellier, France
[6] CIRAD, UMR AGAP, and Inria, F-34398 Montpellier, France
[7] AGAP, Univ Montpellier, CIRAD, INRAE, Montpellier SupAgro, F-34398 Montpellier, France

[†] These authors contributed equally to this work.
* Correspondence: romain.barillot@inrae.fr

Received 27 February 2020; Editorial decision 20 May 2020; Accepted 27 May 2020

Editor: Robert Hancock, The James Hutton Institute, Dundee, UK

Abstract

Shoot architecture is a key component of the interactions between plants and their environment. We present a novel model of grass, which fully integrates shoot morphogenesis and the metabolism of carbon (C) and nitrogen (N) at organ scale, within a three-dimensional representation of plant architecture. Plant morphogenesis is seen as a self-regulated system driven by two main mechanisms. First, the rate of organ extension and the establishment of architectural traits are regulated by concentrations of C and N metabolites in the growth zones and the temperature. Second, the timing of extension is regulated by rules coordinating successive phytomers instead of a thermal time schedule. Local concentrations are calculated from a model of C and N metabolism at organ scale. The three-dimensional representation allows the accurate calculation of light and temperature distribution within the architecture. The model was calibrated for wheat (*Triticum aestivum*) and evaluated for early vegetative stages. This approach allowed the simulation of realistic patterns of leaf dimensions, extension dynamics, and organ mass and composition. The model simulated, as emergent properties, plant and agronomic traits. Metabolic activities of growing leaves were investigated in relation to whole-plant functioning and environmental conditions. The current model is an important step towards a better understanding of the plasticity of plant phenotype in different environments.

Keywords: Carbon, functional–structural plant modelling, grass, leaf growth, metabolism, morphogenesis, nitrogen, plant architecture, plasticity.

Abbreviations: AA, amino acids; E_n, emergence of leaf *n*; FSPM, functional–structural plant model; GAI, green area index; GLN, green leaf number; *hz*, hidden part of the growing phytomer; MS, main stem; MTG, multiscale tree graph; PARa, absorbed photosynthetically active radiation; PTQ, photothermal quotient; RER, relative elongation rate of the leaf during the first phase of extension; RUE, radiation use efficiency; SLA, specific leaf area; SLN, specific leaf nitrogen; SSM, specific structural mass;3D, three-dimensional.

Introduction

Reconciling productivity and sustainability in the context of global change is a critical challenge that agriculture has to face. Mechanistic models can explore plant behaviour in present and future climates, thus allowing investigation of the benefits and drawbacks of novel crop management as well as the identification of plant traits that can be potential targets for plant breeding. For this purpose, models should provide a holistic view of whole-plant functioning by integrating the interactions between environmental factors, morphogenesis, and source–sink activities within the plant. Functional–structural plant models (FSPMs) have opened up possibilities to account for these plant–environment interactions through a realistic description of individual plant architecture (Prusinkiewicz, 1998; Godin and Sinoquet, 2005). Using an explicit representation of the individual variability and heterogeneity of resource availability, this approach provides a framework for understanding and integrating the mechanisms of plant competition and growth in a large range of agronomic situations (Vos *et al.*, 2010; DeJong *et al.*, 2011; Barillot *et al.*, 2014; Sievänen *et al.*, 2014; Gaudio *et al.*, 2019). FSPMs are based on a broad diversity of paradigms, ranging from empirical descriptions of growth to process-based approaches accounting for the trophic status of plants. Among the latter, most crop FSPMs consider only carbon (C) and are based on a supply:demand approach, in which resource allocation among organs is driven by sink priorities defined from empirical relations. Only a few models address the question of supply feedbacks on demand size (Luquet *et al.*, 2006), and key nutrients such as nitrogen (N) and water are rarely considered (Bertheloot *et al.*, 2011; Lobet *et al.*, 2014; Coussement *et al.*, 2018). For the sake of simplicity, existing models use as inputs key traits, which are actually emerging properties of plant functioning and vary with growth conditions. For example, since the rate of shoot development is relatively stable in thermal time (McMaster, 2005), most models have a phyllochron parameter to drive the duration of leaf elongation, while it has been shown that phyllochron may increase with C, N, or water stresses (Cutforth *et al.*, 1992; Longnecker *et al.*, 1993; Muller and Martre, 2019). From a mechanistic point of view, leaf extension drives the phyllochron rather than the opposite. Another example is the relationship between leaf mass and dimension, commonly included in models by using a constant specific leaf area (SLA), while SLA may in fact strongly vary between environments (Rawson *et al.*, 1987; Tardieu *et al.*, 1999; Poorter *et al.*, 2009). Such approximations can lead to large errors in the predictions of plant surface or biomass production. Finally, as pointed out in the review of Poorter *et al.* (2013), we still lack mechanistic modelling approaches simulating whole-plant functioning and trait acquisition as properties arising from the feedbacks between morphogenesis, environmental factors, and source–sink activities within the plant.

For grasses, leaf growth has been extensively studied in terms of (i) histology, (ii) coordination between the elongation of successive leaves, and (iii) regulation by the trophic status. The growth zone is located at the leaf base, inside the pseudostem made of previous sheaths (Begg and Wright, 1962), where cells move through division, elongation-only, and mature zones (Williams, 1975; Skinner and Nelson, 1995; Durand *et al.*, 1999). The length of the zone hidden in the pseudostem strongly influences the elongation of the growing leaf and also impacts the following leaves. Synchronies between emergence events out of the pseudostem and major changes in the kinetics of leaf elongation have been repeatedly documented and formalized as coordination rules in models to account for a self-regulation of plant architecture (Durand *et al.*, 1998; Fournier *et al.*, 2005; Verdenal *et al.*, 2008; Zhu *et al.*, 2014; Vidal and Andrieu, 2019). Finally, a large number of studies have demonstrated the plasticity of leaf dimensions and the correlation of this plasticity with C and N content in the growth zone through an effect on the rate of cell division and/or elongation (Kemp, 1980; Volenec and Nelson, 1984; Schnyder and Nelson, 1987; Gastal and Nelson, 1994; Fricke, 2002).

The present paper describes a model of whole-plant functioning of grass based on a mechanistic representation of leaf growth. The main challenge was to identify a generic frame based on the existing knowledge of leaf growth integrating the effects of environmental conditions. The model relies on an explicit description of plant architecture and two core hypotheses. First, leaf elongation rate and key leaf traits are regulated by the concentrations of C and N metabolites in the growth zone. Second, the transition between successive phases of elongation is triggered according to coordination within and between phytomers. Recently, we have developed CN-Wheat, an FSPM simulating C and N metabolism during the post-flowering stages in wheat, that is, for a static shoot architecture (Barillot *et al.*, 2016*a*). For the present work, we focused on the implementation of a leaf growth model in CN-Wheat. The description of the metabolism was thus extended to the growth zone of leaves. Interactions of plants with environmental factors were calculated from a dynamic representation of leaf geometry. We evaluated the model's ability to simulate leaf growth and key traits at leaf and plant scale. Finally, we explored the sink–source relations in a growing plant.

Materials and methods

Model description

The present work describes a generic frame to simulate the source–sink relations in interaction with the development of plant architecture and local environmental factors. The present implementation focuses on the early stages of development of winter wheat (*Triticum aestivum)* from the exhaustion of grain reserves to the beginning of stem elongation, that is, when leaf and root growth are the main morphogenetic processes. Later stages are not simulated because this would require accounting for tiller regression, which was beyond the scope of this work. The following sections provide an overview of the whole-plant model before focusing on the main assumptions related to leaf growth and metabolism. Finally, we describe the calibration and evaluation of the model. Detailed equations and parameters are available in Supplementary Data S1 at *JXB* online (Protocol S1.1). The terms used in this paper to describe the morphology and development of grasses and model components are defined in Supplementary Data S3.

Overview of the model

Botanical structure of the model The model can simulate an individual plant or a canopy, described as a collection of plants. A plant is composed of one or more tillers. As a provisional choice, all tillers share a single root compartment and a single metabolite pool without explicit spatial representation (hereafter called *phloem*; this does not intend to spatially represent the phloem tube of the living plant but instead mimics the functioning of this organ) allowing fluxes of mobile metabolites among organs. Each tiller has several growing and mature phytomers, each consisting of a leaf (consisting of a lamina and a sheath) and an internode. The number of phytomers increases during the simulation as new phytomers are initiated. In a growing phytomer, the growth zone, located inside the pseudostem, is represented by one single compartment, denoted *hz* (for hidden growth zone). Each type of mature tissue produced by the growth zones (lamina, sheath, or internode) is represented by one or two compartment(s) because we distinguish between the enclosed and exposed tissues to account for their contrasting light regimes.

Morphogenesis In our approach, leaf growth is driven by (i) local metabolite concentrations, which depend on the source–sink relations and the environmental conditions, and (ii) coordination rules between successive leaves: that is, leaf elongation follows a two-phase kinetics and the emergence of a leaf outside the pseudostem triggers the phase transition for the following leaf. Although internode extension is limited for the stages addressed here, their growth has been implemented and partially calibrated (Supplementary Data S1: Protocol S1.1). Briefly, the modelling of internode elongation follows the same principles as for leaves, except that for internodes the phase transition is triggered by leaf ligulation. Additionally, an empirical sub-model of tillering was implemented (Supplementary Data S1: Protocol S1.1) to account for self-shading between tillers and tiller growth costs (Williams, 1964). Tiller emergence is coordinated with the emergence of leaves on the main stem (MS), and their botanical organization, metabolism, and growth dynamics were approximated from that of the MS.

Metabolism The model accounts for different groups of state variables for each organ: dimensions (length, maximum width), structural mass, which is the dry mass 'immobilized' mainly in the cell wall compounds, and concentrations of mobile metabolites [sucrose, nitrates, amino acids (AA)] and storage metabolites (starch, fructans, proteins). Metabolite dynamics are described by differential equations reflecting the physiological activities occurring in the shoot (e.g. photosynthesis, C and N synthesis/degradation, *phloem* loading, growth, tissue death) and roots (e.g. N uptake, *phloem* unloading, transport of nitrates to the shoot, exudation, growth, tissue death). Both metabolite concentrations and the physical environment of each organ drive these activities. Compared with the initial version of CN-Wheat, new metabolic regulations by temperature were implemented for *phloem* conductivity and the rates of synthesis and degradation of metabolites (see Supplementary Data S1: Protocol S1.2).

Implementation Based on a modular composition described in Barillot *et al.* (2019), the current model is composed of (Fig. 1): (i) sub-models of leaf, internode, and root growth; (ii) a dynamic representation of the three-dimensional (3D) geometry of plants, which extends the ADEL-Wheat model (Fournier *et al.*, 2003; Supplementary Data S1: Protocol S1.3); (iii) a sub-model of light distribution within 3D canopies (Chelle and Andrieu, 1998); and (iv) sub-models simulating photosynthesis, N acquisition, synthesis and allocation of C and N metabolites, and senescence at the organ level, which extends the initial version of CN-Wheat (Barillot *et al.*, 2016*a*). Model inputs are hourly climatic conditions (temperature, light, humidity, CO_2, wind), initial soil NO_3^-, and initial dimensions, mass, and metabolic composition of individual organs at the seedling stage. The whole composition is implemented in the OpenAlea platform (Pradal *et al.*, 2008, 2015) as a set of modular sub-models communicating via a central data structure, the multiscale tree graph (MTG) (Fournier *et al.*, 2010; Garin *et al.*, 2014; Albasha *et al.*, 2019; Barillot *et al.*, 2019; Reyes *et al.*, 2019). The code is open source, available on GitHub (https://github.com/openalea-incubator/WheatFspm), and released under a CecILL-C license. The archive of the code used to generate the present results is available at http://doi.org/10.5281/zenodo.3759714.

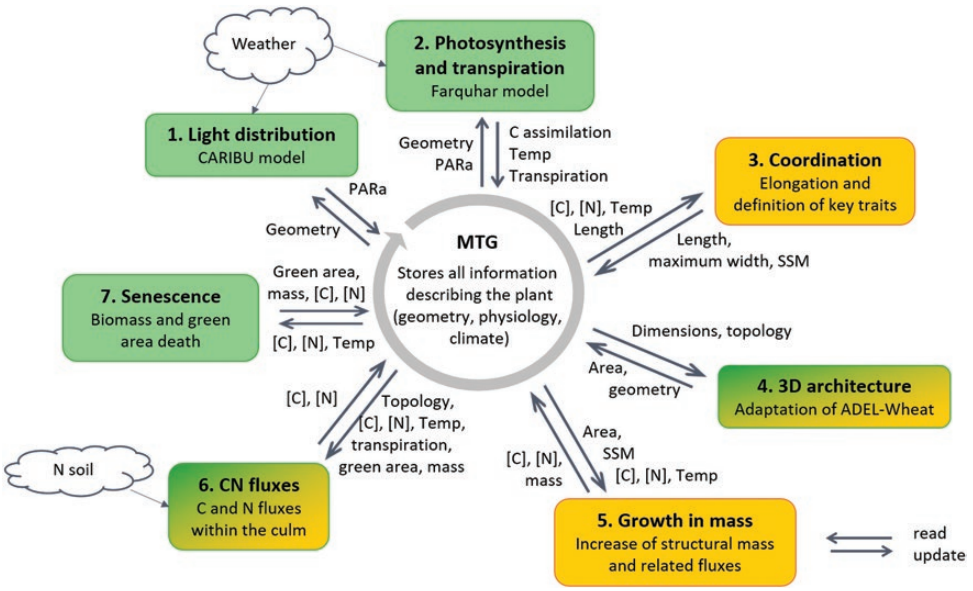

Fig. 1. Coupling of several sub-models using the multiscale tree graph (MTG) formalism as a central data structure. Boxes 1, 2, and 7 are sub-models that already existed (Barillot *et al.*, 2016*a*), boxes 3 and 5 are newly developed sub-models to integrate plant growth in dimensions and mass, and boxes 4 and 6 are former sub-models that were adapted to model a growing plant. The numbering refers to the order in which the sub-models are called for the simulations. Briefly, the light distribution sub-model calculates the fraction, *f*PAR, of incident photosynthetically active radiation (PAR) absorbed by each phytoelement of the plant, from the 3D architecture of the plant and the light sources. The absolute absorbed PAR (PARa) is then calculated from the incident PAR and *f*PAR. The photosynthesis and transpiration sub-model calculates C acquisition, transpiration rate, and organ temperature (Temp). The coordination sub-model calculates the elongation (increase in length) of the leaves and internodes, as well as other key traits [maximum leaf width, specific structural mass (SSM)] based on the current status of the organs in term, of length, metabolite concentrations ([C], [N]), and Temp. The sub-module ADEL then updates the 3D architecture, which results in an increase in area. The increase in structural mass of the shoot organs is calculated from their increase in area and SSM. Based on the above-mentioned calculations, a solver of ordinary differential equations computes N acquisition, reactions of synthesis and degradation, and C and N fluxes. Finally, the senescence is calculated from the protein concentration and the age of each organ. (This figure is available in colour at *JXB* online.)

Detailed assumptions of the leaf growth sub-models

Leaf primordia are initiated according to a constant rate modulated by temperature. The plastochron and the final number of leaves are model parameters, as are the initial length, structural mass, and composition of a primordium.

Structure of the growing leaf Before emergence, the leaf is represented only by a *hz* compartment (Fig. 2). After emergence, the growing leaf is represented by a *hz*, an emerged lamina and, later, by an emerged sheath compartment. At the end of leaf elongation, the *hz* compartment is superseded by an enclosed mature sheath compartment, created with the same dimensions, structural mass, and metabolites as the former *hz*.

For the sake of simplicity, the growing zone was identified as the hidden part of the growing leaf, and thus was represented by the *hz* compartment. This is a simplified representation of the reality, as the hidden part of a growing leaf actually encompasses a dividing and an elongating zone, plus some mature tissues. Moreover, no distinction was made between lamina and sheath. We assumed that the *hz* is supplied with C and N by the *phloem* and by emerged leaf tissues if any are present (Fig. 3). The *hz* is attributed a structural mass variable (including structural N), as well as mobile (sucrose and AA) and storage (fructans and proteins) metabolites. The metabolism of the emerged lamina and sheath tissues is the same as that of mature photosynthetic organs, except that the former export C and N towards their own *hz*.

Regulation of leaf growth in mass and dimensions by C and N metabolism and coordination rules Fournier *et al.* (2005) reported that, starting from one phyllochron before its emergence, the normalized length of wheat leaves increases according to a common pattern for all phytomers when expressed in phyllochronic time, that is, thermal time normalized by the rate of leaf emergence (Fig. 4). We also observed this property on two supplementary datasets (Malvoisin, 1984; Ljutovac, 2002; data not shown). Based on these observations, we modelled leaf elongation kinetics as two successive phases, with the transition between the phases being coordinated with the emergence of the previous leaf. The emergence of leaf n will be denoted E_n hereafter. The model is briefly described below (see Supplementary Data S1: Protocol S1.1 for details of the equations describing leaf growth).

Throughout the first phase (Fig. 5, phase I), which mainly encompasses the formation of the cell division zone, leaf length follows an exponential-like function whose relative elongation rate (RER) is driven by (i) the concentrations of sucrose and AA in the *hz*, (ii) temperature, and (iii) leaf rank, which determines the maximum RER. The increase in leaf structural mass is estimated from an empirical relationship with leaf length, fitted from anatomical observations (Williams and Rijven, 1965). As the leaf grows, it will emerge from the pseudostem formed by previous leaves. This event is central in our approach, since E_{n-1} triggers the transition from the first to the second elongation phase of leaf n (Fig. 5).

Throughout the second phase (Fig. 5, phases IIa–IIc), leaf elongation follows a sigmoidal function of leaf physiological age modulated by air temperature (Supplementary Data S1: Protocol S1.2). The sigmoidal function is identical for all leaves and scaled according to leaf length at E_{n-1}. From E_{n-1} to leaf maturity, the leaf length kinetics are almost predefined and only slightly modulated by the concentrations of sucrose and AA in the *hz*. We therefore assumed that the trophic status does not impact on the time required to reach the final length but, rather, the elongation rate has such an effect. The final length of laminae and sheaths are calculated according to an ontogenic sheath:lamina ratio (Dornbusch *et al.*, 2011; Abichou, 2016). Leaf width and SLA are

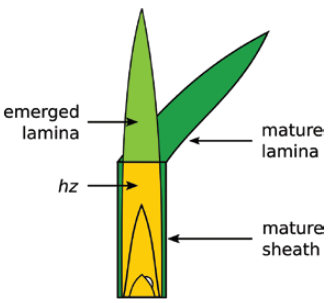

Fig. 2. Structure of a vegetative culm. Three types of compartments are considered: mature photosynthetic organs, the emerged part of the growing organ, and the hidden part of the growing leaf (*hz*). (This figure is available in colour at *JXB* online.)

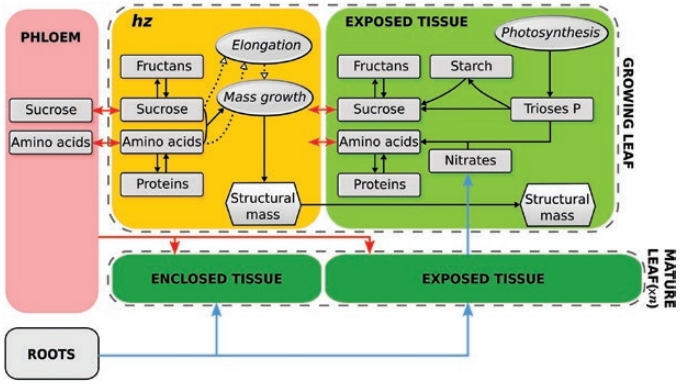

Fig. 3. Representation of the growing leaf and its connections with other plant compartments. The leaf is described as a set of botanical compartments (large rectangles) with structural masses (hexagons) and metabolite concentrations (rectangles). Leaf elongation and mass growth processes (ovals) take place in the hidden growth zone (*hz*) and are regulated (dotted arrows) by local metabolite concentrations. Only exposed tissues are photosynthetic. Fluxes of sucrose and amino acids between compartments, and imports of nitrates and amino acids from the root compartment, are represented by arrows. (This figure is available in colour at *JXB* online.)

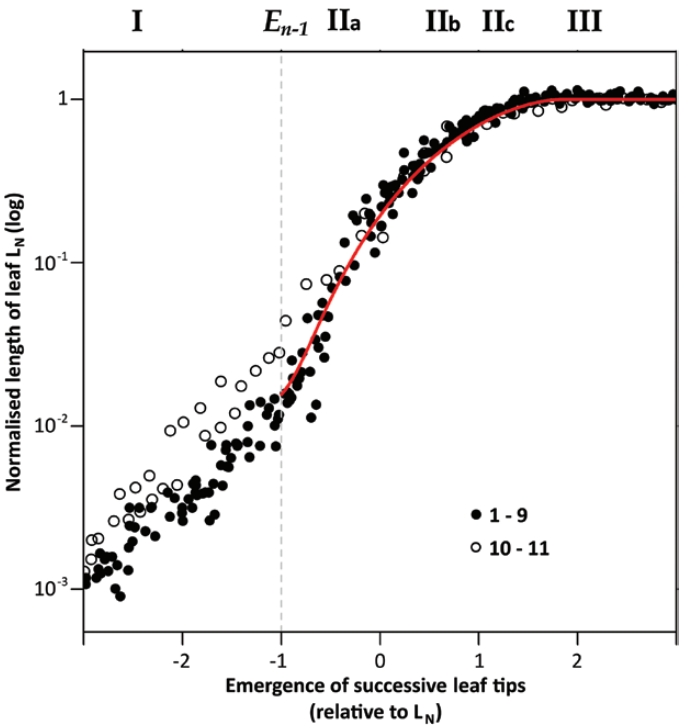

Fig. 4. Normalized length (logarithmic scale) of main stem leaves versus the phyllochronic time relative to leaf emergence (based on Fournier *et al.*, 2005; see Supplementary Data S3 for definitions of terms). Symbols are phytomer rank (11=flag leaf). Each point is the median of 5–10 observations. Numbers above the plot show the main phases of leaf growth, described in the main text and Fig. 5. The dashed line is the emergence of the previous leaf (E_{n-1}), which triggers the transition from an exponential-like elongation (phase I) to a sigmoidal elongation (phase II, solid curve). (This figure is available in colour at *JXB* online.)

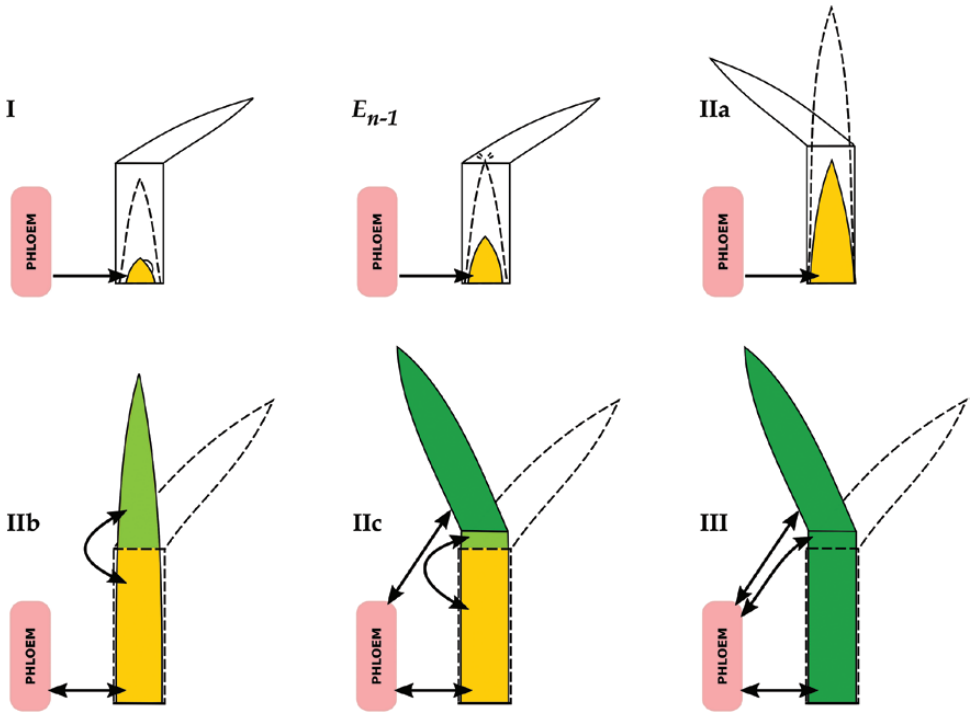

Fig. 5. Illustration of the elongation of leaf *n* (shaded) as represented in the model. See Figs 2 and 3 for identification of the compartments of leaf *n*. The dashed leaf is leaf *n–1*. Only the mature leaf that defines the pseudostem is represented, which is leaf *n–3* in I and E_{n-1}, leaf *n–2* in IIa, and leaf *n* in IIb, IIc, and III. For simplicity, internodes are not shown. I: From the initiation of leaf *n* to the emergence of the previous leaf (E_{n-1}), leaf *n* is a primordium surrounding the shoot apical meristem. Leaf *n* is represented as a homogenous hidden growth zone (*hz*), which imports metabolites from the *phloem* and follows an exponential-like growth. At $E_{n-,1}$ several key variables of leaf *n* are set and sigmoidal elongation starts. IIa: Leaf *n* is fully hidden inside the pseudostem and elongates according to its predefined sigmoidal function. IIb: The emerged lamina exchanges metabolites exclusively with the *hz*. IIc: The lamina is mature and now connected to the *phloem*. The sheath is still growing; its emerged part exclusively exchanges metabolites with the *hz*. III: The leaf is fully mature. The former *hz* is now the mature hidden part of the sheath. (This figure is available in colour at *JXB* online.)

important traits that vary with growth conditions, in particular light availability (Friend *et al.*, 1965; Kemp, 1981; Schnyder and Nelson, 1989; Fournier *et al.*, 2001). We hypothesized that the variability reported in response to light conditions originated from a response to local C availability (Bertin and Gary, 1998). We also considered that variations in SLA partly originated from variations in specific structural masses (SSMs) of laminae (g m^{-2}) and sheaths (g m^{-1}). In order to simply account for this plasticity, the maximal leaf width and the SSMs of laminae and sheaths are calculated at E_n according to the sucrose concentration in the *hz* averaged over the previous two phyllochrons. The structural masses of the emerged laminae and sheaths are then dynamically calculated from their respective SSMs and dimensions. Lamina shape and area are calculated according to lamina length, maximal width, and rank (Dornbusch and Andrieu, 2010). Once the leaf is fully mature (Fig. 5, phase III), the former *hz* is considered as the mature hidden part of the sheath.

Carbon and nitrogen metabolism of the growing leaf The model of leaf elongation requires an explicit description of metabolite distribution at organ scale in order to provide the local concentrations of sucrose and AA that regulate the elongation rate and the key traits described in the previous section. In turn, we assume that the growth area and SSMs drive the structural mass synthesis and subsequent consumption of *hz* metabolites. The cost is calculated by assuming a constant fraction of C and N in the structural mass. Growth respiration also consumes sucrose according to a constant yield (Thornley and Cannell, 2000). Fluxes of sucrose and AA between the *phloem* and the *hz* follow diffusion laws, with conductance depending on the *hz* structural mass and temperature. After leaf emergence, we considered that the emerged tissues export sucrose and AA to their related *hz*. At maturity, the sheath and lamina directly load sucrose and AA into the *phloem* according to the transport formalism described in Barillot *et al.* (2016*a*).

Storage pools of C (fructans) and N (proteins) have also been attributed to *hz* (Schnyder *et al.*, 2000). As for photosynthetic tissues, the synthesis and degradation of fructans depend on their local concentration and the sucrose concentration (Barillot *et al.*, 2016*a*). The rate of protein synthesis is calculated from a Michaelis–Menten function of AA concentration. Since Gastal and Nelson (1994) noted that protein deposition mainly occurred in the division zone of growing tall fescue leaves, we introduced a dependency of the maximal rate of protein synthesis to a length ratio representing the size of the division zone in the *hz*.

The mature leaf

Once growth is complete, the leaf consists of a mature lamina and sheath, whose metabolisms are described in Barillot *et al.* (2016*a*). The model also accounts for tissue death (Supplementary Data S1: Protocol S1.1). At each time step, a constant fraction of green area is lost if (i) protein concentration decreases below a fraction of the maximum protein concentration reached after leaf ligulation (Barillot *et al.*, 2016*a*) or (ii) the physiological age is higher than a fitted threshold (which applies only to laminae). The structural mass of the remaining green tissues is reduced proportionally to the green area, while a fraction of storage metabolites is remobilized towards the green tissue as sucrose and AA.

Model evaluation procedure

The whole-plant model was run to simulate a wheat plant from the emergence of leaf 4 to the beginning of stem elongation (2500 h). The model was run with an hourly time step, except for the 3D representation of the canopy, which was updated every 4 h. This means that the absorbed PAR was calculated from hourly values of incident PAR, applied to a

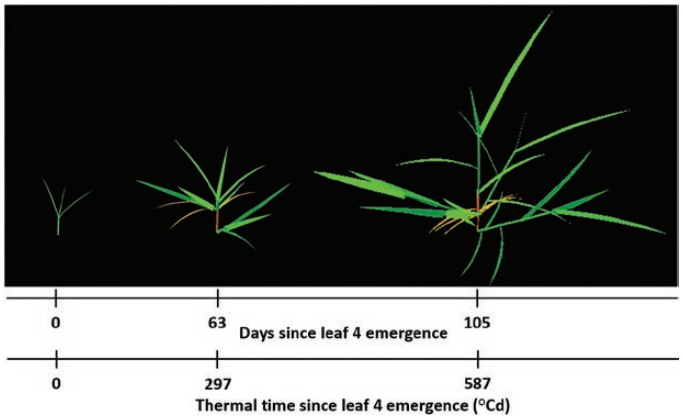

Fig. 6. 3D shoot architecture of a plant at three simulation steps. At day 63 and day 105, three and five leaves of the main stem were fully senescent, respectively. (This figure is available in colour at *JXB* online.)

structure updated every 4 h, to limit the computational cost of the calculation of the distribution of light between phytoelements.

Simulations were compared with three complementary experimental datasets (Exp1–Exp3; Supplementary Data S1: Protocol S1.5) representative of optimal field conditions in north-western Europe. Detailed experimental data allowing comparisons with model outputs for identical conditions were available only for a few traits; the other traits were evaluated qualitatively, using data collected for various stages of development, grass species, or growth conditions. The whole model gathers approximately 160 parameters, some of which were set in the post-flowering version of CN-Wheat (Barillot *et al.*, 2016*b*), while new parameters were pragmatically calibrated or taken from the literature (Supplementary Data S1: Table S1.2). Plant density was set to 250 plants m^{-2} and soil $NO_3^-$was initialized at 6 g m^{-2}. To simulate fertilization of Exp1, soil $NO_3^-$was increased by 5 g m^{-2} at t=2016 h. We used hourly weather data (temperature, incident PAR, humidity, and wind speed) from Exp1 (Supplementary Data S2: Fig. S2.1); atmospheric CO_2 concentration was set at 360 ppm. Initialization of the state variables for each organ was performed from data of Exp1–Exp3. The detailed procedures for parameter calibration and model evaluation are presented in Supplementary Data S1 (Protocol S1.5).

Results

Fig. 6 and Supplementary Video S1 illustrate the simulated growth of a plant from E_4 to ~E_9. First, we assessed the ability of the model to simulate some major leaf traits and realistic dynamics of shoot development. Second, we evaluated whether agronomic traits, usually observed at canopy level, emerge from the integration of the local processes simulated at organ scale. Finally, we investigated the sink–source relations within the plant, with a particular focus on C.

Dynamics of shoot development

The model accurately predicted the increase in the final length of leaves and sheaths with foliar rank observed in Exp1 (Fig. 7A). In the model, variations of final leaf length with the metabolic status and environmental conditions are generated by variations of the duration of the exponential growth prior to E_{n-1} (phase I) and of the elongation rate (mainly during phase I). Leaf RER observed in Exp1 markedly decreased with leaf rank (Fig. 7B), which is in line with studies reporting that multiple primordia of wheat leaves elongate synchronously with

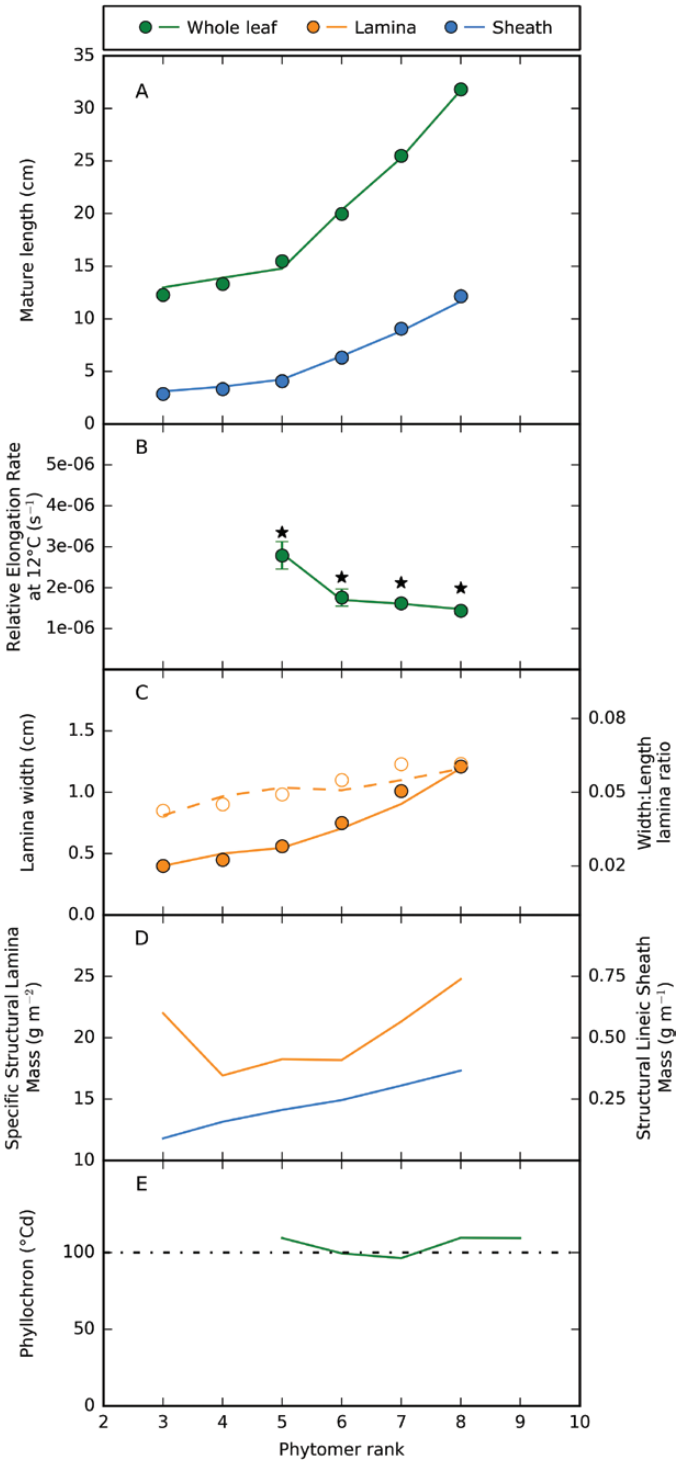

Fig. 7. Leaf traits on the main stem. (A) Final length of the whole leaf and of the sheath. Simulations are represented by solid lines and experimental data (Exp1) are represented by dots (confidence intervals of observed lengths are smaller than symbols). (B) Average RER of leaves during the first elongation phase, calculated from simulations (solid curve) and experimental data (Exp1, dots). Vertical bars represent the 95% confidence intervals. Confidence intervals for simulated RER are not shown (<1e^{-8}). Asterisks indicate the maximal RER (see Supplementary Data S1: Table S1.2 for model parameters). (C) Maximal lamina width simulated (solid line) and observed (filled circles); the dotted line and open circles are the simulated and observed ratio between lamina maximal width and final length (no confidence interval is available for width observations). (D) Specific structural lamina mass and structural lineic sheath mass simulated by the model. (E) Simulated interval (°Cd) leaf emergence dates. At the end of the simulation, leaf 10 is still hidden in the pseudostem. (This figure is available in colour at *JXB* online.)

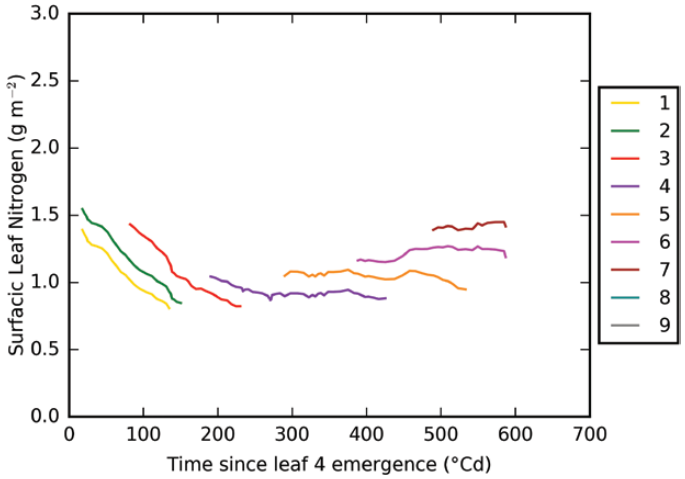

Fig. 8. Specific leaf nitrogen of laminae from leaf ligulation to the start of senescence. Different curves represent the individual phytomers (see right panel for identification). (This figure is available in colour at *JXB* online.)

different RERs (Williams, 1975; Malvoisin, 1984; Ljutovac, 2002). Simulated RERs, which depend on metabolite concentrations in the *hz*, temperature, and leaf rank, were aligned with these observations, ranging from 1.5 to 2.8×10^{-6} s^{-1} (see Supplementary Data S2: Protocol S2.1 for calculations). The model simulates maximal lamina widths from their final length and sucrose concentration in the *hz* (Supplementary Data S1: Eqn. 7), which predicted the increase in maximum lamina width with leaf rank, ranging from 0.4 to 1.2 cm (Fig. 7C).

Overall, the simulated SSMs of laminae and sheaths showed a positive gradient with leaf rank (Fig. 7D), which arose from the dynamics of sucrose concentration in the *hz* and an ontogenic parameter for sheaths. Simulations of metabolic content and structural masses allowed the prediction of specific leaf nitrogen (SLN; Fig. 8) and SLA (Supplementary Data S2: Fig. S2.2B) as an emerging property of the model. SLN varied between 0.8 and 1.5 g m^{-2}, showing at any time a vertical gradient from the lower to the upper leaves. For leaves that emerged after model initiation, the vertical range of SLN increased from ~0.1 g m^{-2} at 200 °Cd to ~0.5 g m^{-2} at 500 °Cd. This is in line with data from the literature; for example, for spring wheat with optimal N fertilization, Dreccer *et al.* (2000) reported a vertical range of SLN of 0.7 g m^{-2} before canopy closure. The SLA of individual leaves increased from emergence to ligulation and was maximal for leaf 4 (~40 m^2 kg^{-1}) and then decreased for the following leaves (leaf 9, ~27 m^2 kg^{-1}).

In our simulations, leaves emerged at relatively stable thermal time intervals (Fig. 7E). On average for all leaves, phyllochron (see Supplementary Data S2: Protocol S2.1 for calculation) was 104 °Cd (95% confidence interval 99–109 °Cd), which is reasonably close to the observations (111 °Cd ±0.7). Phyllochron stability is a major property of the model emerging from coordination rules and the modulation of elongation rates by metabolic concentrations.

The dynamics of the decimal green leaf number (GLN) of the MS (Supplementary Data S2: Eqn. S2.1) were compared with four independent datasets representing three winter wheat cultivars (Abichou, 2016). Experimental data followed typical kinetics (Fig. 9A): GLN first increased up

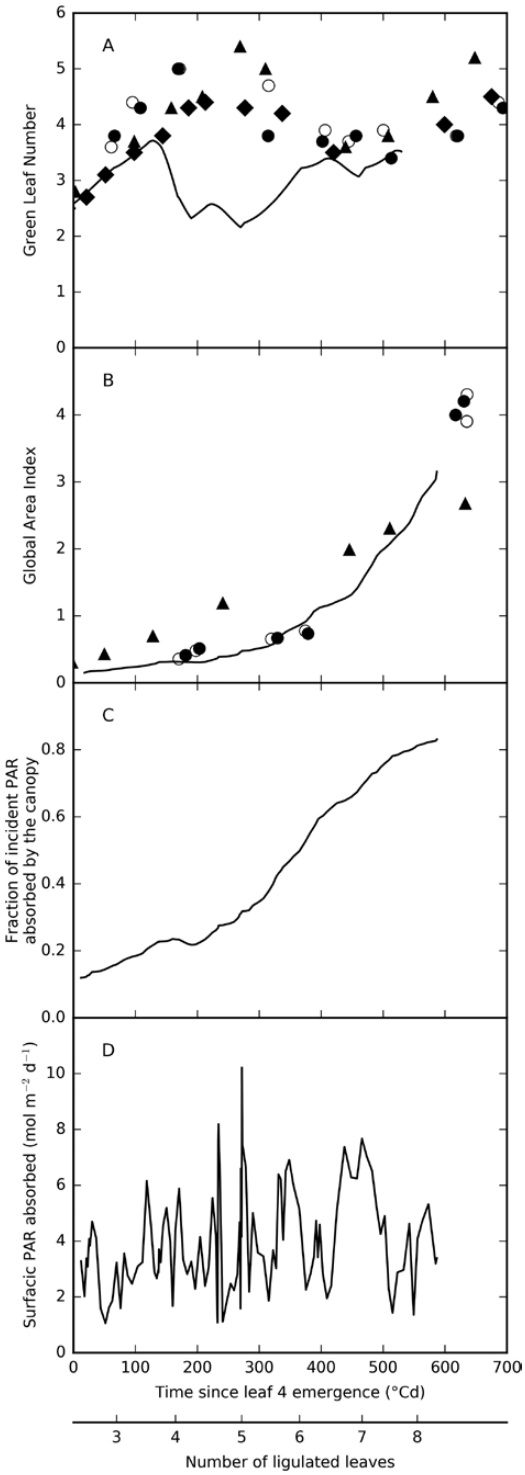

Fig. 9. Dynamics of canopy traits. (A) Green leaf number of the main stem. The solid line shows the simulation. Dots show observations from field experiments (Abichou, 2016) that were conducted with similar agronomic conditions and at the same location as Exp1–Exp3 [filled circles, cv. Soissons 2004/2005 (Exp2); open circles, cv. Caphorn 2004/2005; diamonds, cv. Maxwell 2010/2011; triangles, cv. Caphorn 2013/2014]. (B) Global area index of the whole plant. The solid line shows the simulation. Dots show observations from field experiments (Abichou, 2016), which were conducted with similar agronomic conditions and at the same location as Exp1–Exp3 (filled circles, cv. Soissons 2012/2013; open circles, cv. Caphorn 2012/2013; diamonds, cv. Maxwell 2010/2011). (C) Simulation of the fraction of incident PAR absorbed by green phytoelements. (D) Simulation of the daily PAR absorbed per area of green phytoelement.

to the ligulation of leaf 5, then senescence began and GLN declined until the ligulation of the fourth leaf from the top (leaf 7 in our simulation). The overall trend of GLN was well captured by the model, although the model anticipated the senescence of leaf 1, which resulted in a transitory underestimation of GLN by one leaf. The senescence of this leaf was triggered by a low N content in the model, meaning that either the N dynamics were not well simulated or the rule for triggering senescence is not adapted to young leaves, or possibly both. Since leaf 1 is small, the photosynthetic area was underestimated by only 12% at that time (Supplementary Data S2: Fig. S2.2A).

The simulation of the green area index (GAI) (Supplementary Data S2: Eqn. S2.2) followed an exponential dynamics (Fig. 9B) aligned with observations for cv. Soissons and Caphorn. Increases in GAI in the model resulted from the development of leaves on the MS and the tillers. In the present simulation, four primary tillers have emerged following the concept of cohorts. At the end of the simulation, the canopy reached a GAI of 3 and ground cover, represented by the fraction of incident PAR absorbed by the canopy, was above 0.8, indicating canopy closure (Fig. 9C). The close agreement between observed and simulated GAIs means that the estimates of absorbed PAR were calculated from realistic canopies. The PAR absorbed per unit surface of green tissues (Fig. 9D) showed large daily oscillations but no clear trend during the simulated period (mean ~3.5 mol m^{-2} d^{-1}). Altogether, these results show that the canopy completely changed from a population of isolated plants to a closed canopy with self-shading of the lower leaves (Fig. 9B, C), while mean light availability per unit surface of green tissue did not decrease because of the seasonal increase in light intensity (see Supplementary Data S2: Fig. S2.1B).

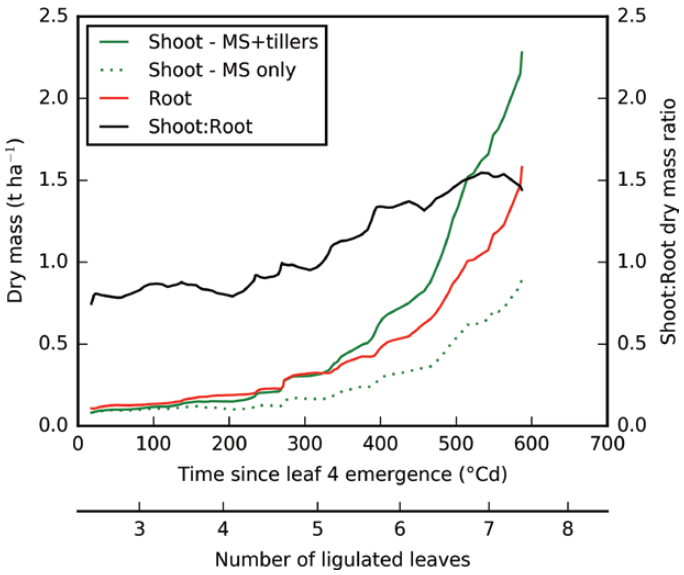

Fig. 10. Simulated dry mass and shoot:root dry mass ratio. (This figure is available in colour at *JXB* online.)

Agronomic traits emerged from the integration of local processes at plant scale

The shoot:root ratio is an important agronomic trait that is strongly determined by gene × environment interactions. Simulated shoot and root biomasses increased exponentially over time (Fig. 10) and the shoot:root ratio increased from ~0.8 at E_4 to ~1.5 at E_9. An increase in the shoot:root ratio during the tillering period is widely acknowledged but lacks accurate quantification. The few studies that have attempted to quantify the whole root system during early growth stages in field conditions (Siddiqi *et al.*, 1990; Kätterer *et al.*, 1993) reported a shoot:root ratio below 1 at the beginning of tillering and then an increase, which is qualitatively in line with our simulations.

Root N fraction decreased from 1.1% at E_4 to 0.7% at E_9, while shoot N fraction was stable at ~4%; these results are reasonably close to the experimental data (Fig. 11), except for the latest date. The overestimate of shoot N at ~550 °Cd is explained by the single N fertilization of 5 g m^{-2} that was applied at ~410 °Cd in the model (as in Exp1), whereas the experimental data shown in the figure are from Exp3, in which only 4 g m^{-2} N were supplied at ~275 °Cd. When expressed as a function of the shoot biomass (Fig. 11, inset), the shoot N fraction was relatively stable.

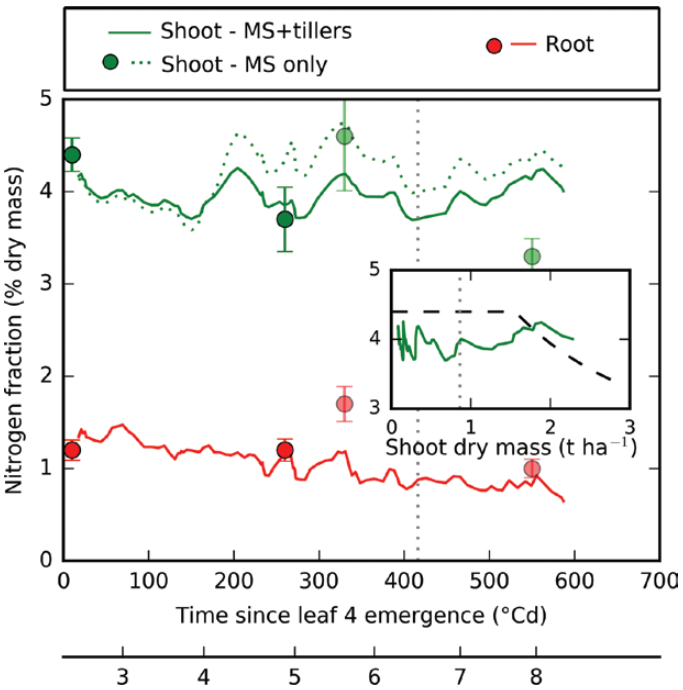

Fig. 11. N fraction of the main stem, whole shoot (main stem+tillers), and roots as a percentage of the dry mass of the compartments. Dots are N fractions of the main stem shoot and large roots as measured in Exp3. Vertical bars represent the 95% confidence interval. The last two (shaded) dots correspond to the measurements performed after 4 g m^{-2} N was applied at 275 °Cd in Exp3 (see Supplementary Data S1: Protocol S1.5) whereas the simulation mimicked Exp1, in which 5 g m^{-2} N was applied at ~410 °Cd (vertical dotted line). The inset shows the whole shoot N fraction together with the critical N dilution curve for winter wheat (dashed line) as calculated by Justes *et al.* (1994). The critical N dilution curve has not been experimentally validated for biomasses <1.5 t ha^{-1}. (This figure is available in colour at *JXB* online.)

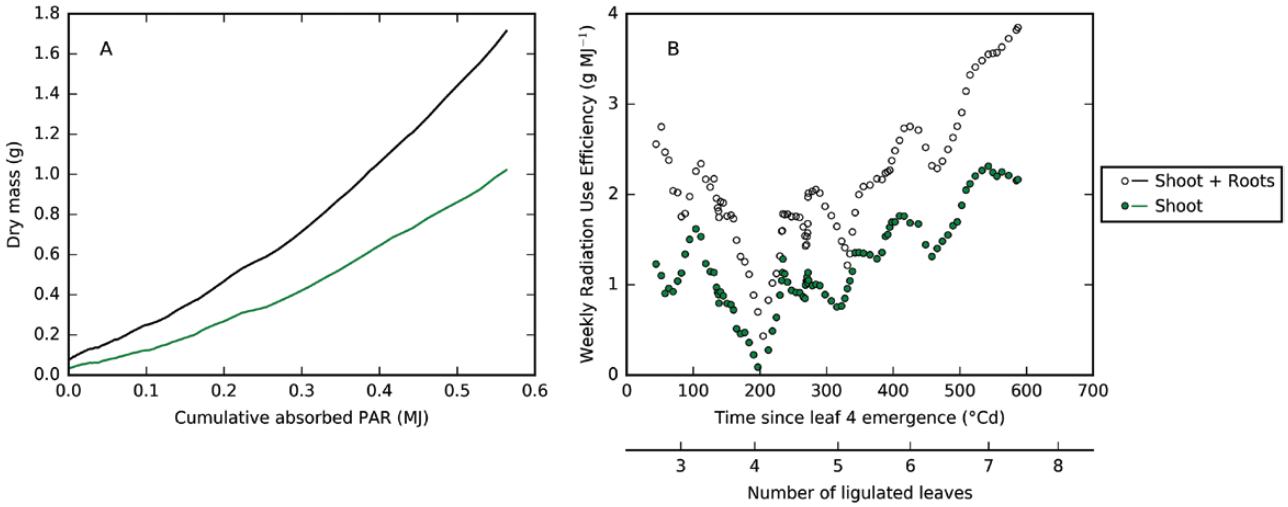

Fig. 12. Radiation use efficiency (RUE) computed from absorbed photosynthetically active radiation (PARa) of the plant. (A) Hourly dynamics of whole-plant dry mass and shoot dry mass as a function of the PARa accumulated from model initialization. (B) Dynamics of weekly integrated RUE. (This figure is available in colour at *JXB* online.)

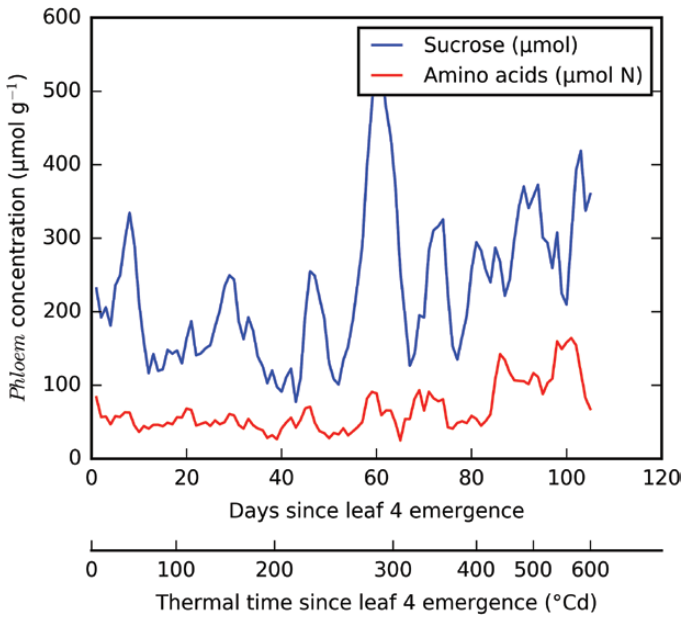

Fig. 13. *Phloem* and hidden growth zone (*hz*) concentrations of sucrose and amino acids. *Phloem* concentrations are calculated as the amount of metabolites of the *phloem* divided by the structural mass of the whole plant. (This figure is available in colour at *JXB* online.)

Over the whole period, the radiation use efficiency (RUE), calculated as the ratio of shoot dry mass to the cumulative PAR absorbed by green tissues, was 1.6 g MJ^{-1}. The literature lacks accurate estimates of RUE for juvenile stages, and experimental studies generally refer to intercepted global radiation estimated from leaf area index using the Beer–Lambert law. Using this method, Calderini *et al.* (1997) reported an average RUE of 1.12 g MJ^{-1} (range 0.98–1.25 g MJ^{-1}) for several cultivars from the double-ridge stage to anthesis. When we precisely reproduced this method, the RUE calculated from our virtual canopy was 1.1 g MJ^{-1}, which is in the middle of the reported range. However, simulated plant and shoot dry masses did not evolve linearly with the cumulative absorbed radiation (Fig. 12A), and the weekly average of RUE varied between 0.1 and 2.2 g MJ^{-1} (Fig. 12B) and was correlated with the photothermal quotient (PTQ) (see Supplementary Data S2: Fig. S2.4; R^2=0.49, P=9.10^{-7}). Variations in shoot:root ratio, respiration, and exudation played minor roles in the increase in RUE simulated from E_4. In our simulation, this trend resulted from an increase in photosynthesis efficiency originating from higher leaf temperature and N content.

Investigating growth costs with respect to plant trophic status

Plant trophic status

The concentrations of sucrose and AA in the *phloem* represent the amounts of mobile C and N that can flow between sources (mainly mature leaves) and sinks (mainly roots and growing leaves). Due to low flux resistance, sucrose and AA concentrations in growing leaves (i.e. the *hz*) were at equilibrium with those in the *phloem*, ranging from ~100 to 550 µmol g^{-1} for sucrose and ~50 to 180 µmol g^{-1} for AA (Fig. 13). The sucrose concentration showed large variations over periods of a few days, which could be associated with changes in the PTQ (Supplementary Data S2: Fig. S2.1C). This reflects that short-term changes in light and temperature markedly affected the source–sink balance and the availability of metabolites in the plant. Over the whole simulation period, however, PTQ explained 46% of variations in sucrose concentration (P=10^{-7}). Overall, *phloem* concentrations did not show a clear trend during the first 80 days, then sucrose presented an upward trend, which coincided with the increase in RUE (Fig. 12). AA showed a transient rise associated with N fertilization (Supplementary Data S2: Fig. S2.1E).

From leaf heterotrophy to leaf autotrophy

The sink–source balance during leaf ontogeny is illustrated (Fig. 14) for leaf 5, which was held on a short internode, and leaf 8, which was twice as long and twice as wide and held on an internode that will elongate later. When leaves were still hidden inside the pseudostem, they imported small amounts of mobile metabolites from the *phloem* (<2 µmol day^{-1} for sucrose;

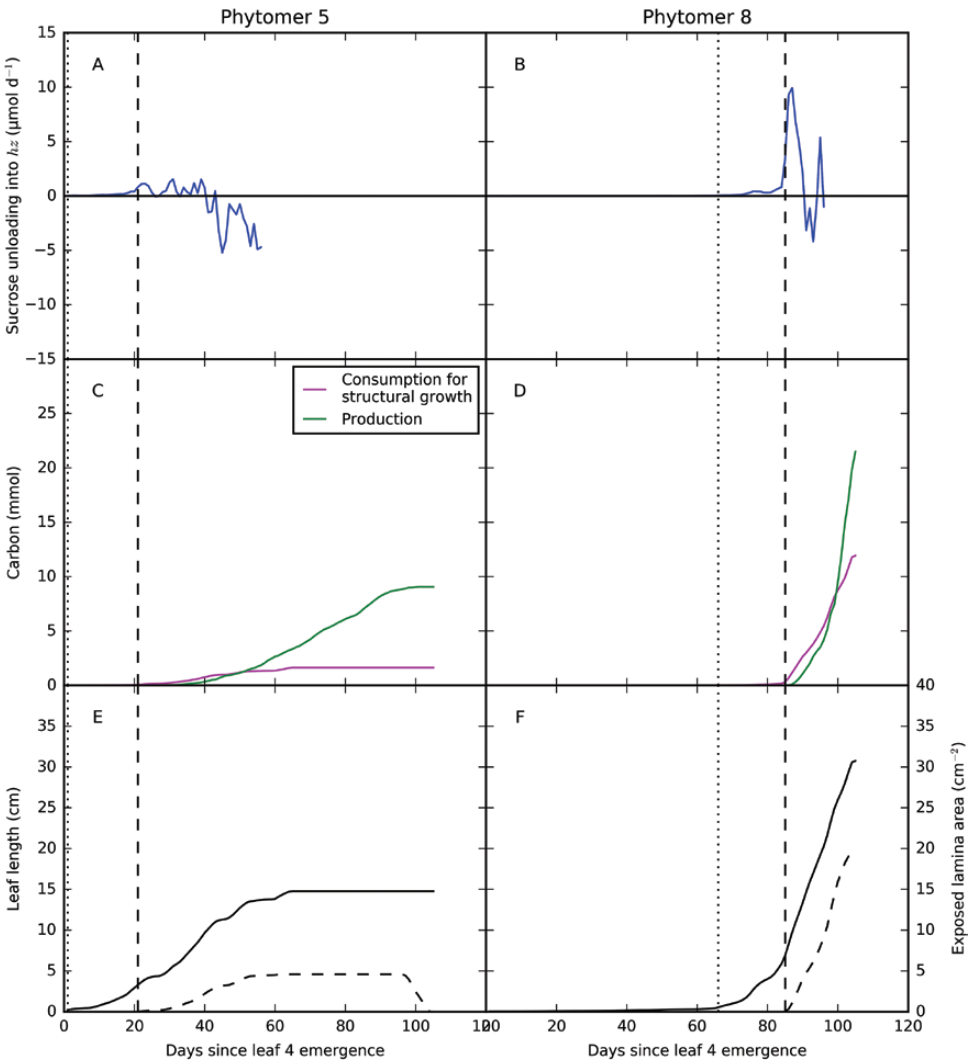

Fig. 14. C metabolism of phytomers 5 and 8 in relation to their growth. For the sake of clarity, daily values are shown from the hourly outputs provided by the model. (A, B) Daily fluxes of sucrose from the *phloem* to the hidden part of the growing phytomers (i.e. the *hz*) of the main stem. Positive values indicate unloading of the *phloem* into the *hz*, while negative fluxes represent exports from the *hz* to the *phloem*. The curve is shown as long as the impact of internode growth on *hz* fluxes is insignificant. (C, D) Comparison of C assimilation by the leaf and consumption for structural growth. (E, F) Dynamics of leaf length (solid line) and exposed green area of the laminae (dashed line). The vertical dashed and dotted lines show the time of leaf emergence and previous leaf emergence, respectively. (This figure is available in colour at *JXB* online.)

Fig. 14A, B). The daily imports were larger for leaf 8 than leaf 5, in relation with their respective daily extension (Fig. 14E, F). Leaves 5 and 8 switched from heterotrophy to autotrophy for C respectively 20 and 10 days after emergence, that is, once they had reached ~50% of the final lamina area (Fig. 14E, F). These transition times are consistent with estimates for barley (Dale, 1985) and tall fescue (Bregard and Allard, 1999). The cumulative C consumption for leaf structural growth was 1.6 mmol for leaf 5 versus 11.9 mmol for leaf 8 (Fig. 14C, D). At the end of its life, leaf 5 had produced five times as much C as it had consumed for its structural growth (Fig. 14C). Both leaves reached the point of return on C investment when they were 95% of their final length, which corresponded to the full lamina emergence (Fig. 14E, F).

Carbon usage and growth costs

Over the simulated period, 40% of the assimilated C remained in the shoot (25% for structural growth and 15% in mobile and storage metabolites), 25% was allocated to roots, 27% was lost by respiration, and 8% was lost by exudation (Fig. 15A). The fraction of C allocated to shoot structural growth tended to increase with time, in accordance with the dynamics of the shoot:root ratio (Fig. 10). The simulated trend of C allocation is aligned with experiments on wheat based on ^{14}C pulse-labelling, which reported an increasing fraction of net assimilated C allocated to the shoot over the growing season (reviewed in Swinnen *et al.*, 1995). During our simulation, 60% of the C allocated to the roots remained in the biomass, while 40% was lost through respiration and exudation. Experiments on wheat during tillering reported up to 60–75% of losses through these processes (Keith *et al.*, 1986; Swinnen *et al.*, 1995), which indicates that our model may underestimate root respiration and exudation, perhaps because it does not consider root turnover for the vegetative stages. Daily, growing leaves (MS+tillers) imported on average 20% of the C available in the *phloem* (Fig. 15B), which also represented 20% of daily photosynthesis (Fig. 15C).

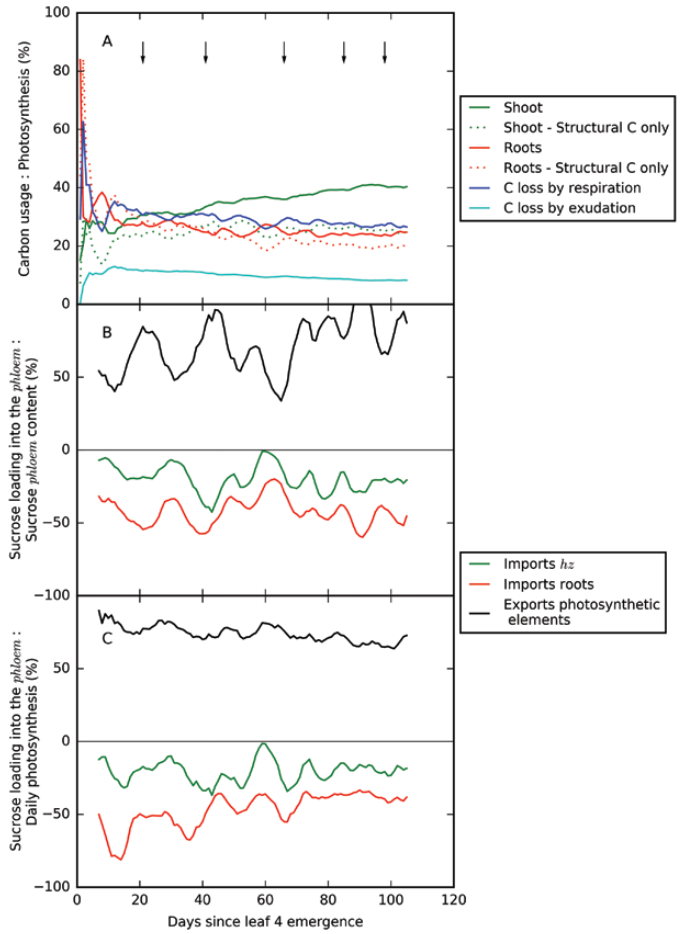

Fig. 15. C source–sink relations of the whole plant. (A) Cumulative C usage as compared with the cumulative C absorbed by photosynthesis. (B, C) Daily fluxes of sucrose into the *phloem* as compared with the sucrose *phloem* content (B) and the C absorbed by photosynthesis daily (C). Values are smoothed as the rolling mean of the previous 7 days. The curves for the imports of the hidden part of the growing phytomer (*hz*) relate to its heterotrophic stage only. Arrows indicate leaf emergence. (This figure is available in colour at *JXB* online.)

Roots were a major sink, daily importing ~40% of the C from the *phloem* (Fig. 15B). On average, sinks consumed 70% of the C from the *phloem* each day, but photosynthesis maintained a high C content in the *phloem* (Fig. 13), indicating a high C turnover. The source–sink relations were relatively stable over the simulated period, despite marked changes in the canopy structure (Fig. 9) and climatic conditions. The strong daily variations observed in Fig. 15B and C resulted from variations both in fluxes and in *phloem* sucrose concentrations. Over the simulated period, C influxes became higher than effluxes (Fig. 15C), which resulted in an increase in non-structural C in both shoot and roots (Fig. 15A).

Discussion

Current models largely integrate predefined behaviours based on observations that may not be representative of novel situations (Poorter *et al.*, 2013). Mechanistic approaches may predict these behaviours as emerging properties and therefore account for their flexibility. This has recently motivated a large body of literature calling for the building of models closer to biological knowledge (Boote *et al.*, 2013; Muller and Martre, 2019) while maintaining a sufficient level of parsimony (Hammer *et al.*, 2019). With this in mind, we developed an individual-based model integrating shoot morphogenesis with C and N metabolism at the organ level.

We used metabolite concentrations to drive the behaviour of growth zones, which expresses the view that only local variables drive the local behaviour. This implied accounting for all activities affecting the metabolic budget and transfers within the plant. This also required a whole-plant model explicitly accounting for major metabolic costs including respiration and exudation. The expression of growth response to local concentrations, the growth-related costs in metabolites, and the response to temperature are novel features compared with the initial version of CN-Wheat. The regulation of leaf growth timing by coordination rules is another essential assumption, which expresses the idea that the mechanics of the whole plant body builds, rather than follows, rhythmic patterns. Such a view has been previously supported by both experimental and modelling papers (Casey *et al.*, 1999; Fournier *et al.*, 2005; Andrieu *et al.*, 2006; Verdenal *et al.*, 2008; Zhu *et al.*, 2014; Vidal and Andrieu, 2019). However, this is the first time such coordinations have been considered jointly with growth costs and modulations of extension rates by the plant status. We demonstrated the concept by simulating the early stages of wheat growth.

The model simulated as emerging properties plant traits that are usually model inputs

Coordination rules in which the emergence of a leaf triggers the rapid extension of the next growing leaf resulted in a regular rate of leaf appearance (Fig. 7E). This mechanism played a pivotal role in predicting the increase in size between successive leaves (Fig. 7A).

In our model, RUE is an emerging property of C (and N) budget, based on the balance between the acquisition of C by photosynthesis and loss by respiration and exudation. The average RUE calculated over the simulation period almost exactly matched experimental values reported for similar conditions. RUE is known to vary markedly with ontogeny, temperature, light conditions, and crop nutrition, and is considered a major target for raising yield potential (Parry *et al.*, 2011; Slattery and Ort, 2015). Some RUE-based models include part of these dependencies (Boote *et al.*, 2013) but experimental assessment is difficult to achieve because increases in biomass can be accurately measured only over long periods of time. When considering weekly intervals, simulated RUEs varied from 0.10 to 2.2 g MJ^{-1} (Fig. 12B) and showed large short-term changes correlated with photosynthesis efficiency (Supplementary Data S2: Fig. S2.4), which was regulated by leaf temperature and N content. CN-Wheat appears to be a tool to disentangle the variability of RUE as a function of plant parameters, ontogeny, and growth conditions.

Over the simulated period, the simulated shoot:root ratio increased from 0.8 to ~1.5 (Fig. 10), which is in line with

the few data published for comparable situations (Lupton *et al.*, 1974; Siddiqi *et al.*, 1990). There are large ontogenetic trends in shoot:root ratio, together with substantial genotypic and environmental variability (Friedli *et al.*, 2019): this variability combined with experimental difficulties makes the shoot:root ratio a major unknown in our understanding of C economy in plants and the C cycle in terrestrial ecosystems. With a mechanistic approach to simulate shoot:root ratio and a conservative stoichiometric budget, our approach represents a further step forward to address these questions.

The N:C ratio is a key variable in plant models. Most crop models (e.g. STICS, APSIM, CERES; reviewed in Zhao *et al.* 2014) and some FSPMs (Louarn and Faverjon, 2018) regulate morphogenesis and N acquisition by comparing the current value of N:C in the plant shoot to a reference value, the critical N concentration. Experimental assessments, however, showed large errors (>100%) in N:C estimated with these models (Coucheney *et al.*, 2015; Faverjon *et al.*, 2019). Plant N consists of diverse compounds that have contrasting dynamics and are involved in different processes, so limitations should arise from aggregating them in a single driving variable. Identifying this complex set of processes in our model resulted in plausible dynamics of N:C (Fig. 11), which emerged from our model, whereas teleonomic approaches use them as a target to drive plant growth.

The model allowed exploration of the functioning of growing grass

The 3D modelling of plant architecture has provided novel insights into the environment perceived by plant tissues, allowing a better understanding of plant functioning (Chelle, 2005). In this work, the simulation of metabolite availability at organ scale marks a further step by providing highlights on internal conditions during the early stages of growth. On the one hand, the model showed substantial changes in metabolite availability over short periods in response to meteorological variations (Fig. 13). On the other hand, over the whole period, the general trend was a moderate increase in sugar availability, despite the increasing plant–plant competition, as GAI was close to 3 at the end of our simulation (Fig. 9B). We could not find bibliographic data for the changes of metabolites during grass development but the trend of increasing C availability is consistent with the fact that the period simulated corresponds to active tillering. C availability is expected to decrease drastically shortly afterwards because of an increasing C demand for stem elongation without an increase in light capture.

The model allowed us to explore the feedback loops between sink and source activities and metabolite availability. Michaelis–Menten responses used in the model mean that when metabolite concentrations are low, this affects all sinks, independently of their size, but, depending on their affinity for substrate, small sinks are affected even when their growth requires extremely low amounts of metabolites. When metabolite concentrations are high, sink activity is regulated by their maximum rate. This implies that sink hierarchy changes depending on substrate availability, which showed considerable change over relatively short periods of time in response to the photothermal ratio. There was a high turnover of mobile metabolites in the plant; photosynthesis provided daily an amount of C representing ~60% (range 30–100%) of the C available in the *phloem* (Fig. 15B), while sinks consumed very slightly less, resulting in increasing C availability. Roots imported daily ~40% of *phloem* C, while leaf growth zones imported daily only ~10% of *phloem* C (Fig. 15B). Leaves were very small sinks before their emergence, and after half the lamina had emerged, their costs were provided by their exposed tissues (Fig. 14).

The model paves the way for improved process description and integration over the whole plant cycle

Our approach provides a new frame to combine morphogenesis with C and N metabolism, and demonstrates its ability to simulate a growing plant. However, the model requires further validation and several components will likely benefit from refinements. The ability of the model to simulate contrasting conditions with a unique set of parameters obviously deserves further investigation. We used a pragmatic approach for parameter fitting; parameters already existing for the post-flowering period were unchanged, except a few for which we made sure that changes did not affect the simulations of the post-flowering period (Supplementary Data S1: Protocol S1.4). Given the large difference in growth conditions between the early-stage and post-flowering periods, correctly simulating both cases is the first evidence of robustness. Further developments are needed to simulate the whole plant life cycle, including tiller dynamics and floral transition.

While having a mechanistic structure, the model assembles a large number of sub-models (Fig. 1), each being a simplified representation of the plant structure and functioning. The present level of detail is a transitory choice, to be refined based on further model assessment and needs. In particular, the root sub-model could be improved by a better description of the root architecture and the root–soil interactions, as well as root growth and senescence, which were empirically calibrated. Another example is the representation of the *hz* as a single compartment, while it actually includes cell division and elongation zones plus some mature tissues. Distinguishing these zones may be necessary to more faithfully represent the processes leading to the definition of leaf width and SLA, at the price of more complexity. In addition, the present implementation uses a predefined ontogenetic trend to simulate the sheath:lamina ratio (Supplementary Data S1: Eqn. 6B), rather than incorporating knowledge about ligule formation and cessation of sheath extension (e.g. Vidal and Andrieu, 2019). This choice may be revised in future versions. Another example is the use of an ontogenetic trend in the maximum RER of leaves during their exponential growth ($RER^{max}_{leaf,\ n}$) (Supplementary Data S1: Table S1.2), while it would have been satisfactory to define a leaf model whose parameters are all independent of leaf rank. Why successive leaves in grasses elongate simultaneously with different RERs has been specifically questioned for a long time (Williams and Williams, 1968; Rogan and Smith, 1975). Our simulation showed no trend of a decrease in the availability in C or N during the simulated period, which

excludes the possibility that differences in RER could simply originate from competition between an increasing number of sinks. The hierarchy between successive primordia seems to still lack a clear explanation, and that is what motivated the description through an ontogenetic trend in our model.

The present implementation is intended as a frame to be complemented to simulate the full pre-flowering period. The first step would be implementing an explicit description of tillers, similar to that taken for the MS. The behaviour of grass tillers, especially factors controlling their emergence and senescence, is a crucial aspect of crop production, but this is only partly understood. Our approach will open opportunities to explore these processes in relation to C and N availability. The model structure (Fig. 1) allows the implementation of new modules; for example, a module for apical meristem would allow simulation of the rate of initiation, the initial properties of phytomers, and the change from vegetative to reproductive phase. Finally, the focus here on C and N does not mean that we assume these variables are sufficient to provide all necessary information in a plant model. However, primary metabolites are obviously key variables that were missing in current models, so we believe the present work is a significant step towards a mechanistic approach of plant modelling.

Supplementary data

Supplementary data are available at *JXB* online.

Data S1. Model description.

Data S2. Model evaluation.

Data S3. Glossary.

Video S1. Top view of the simulated 3D canopy from leaf 4 emergence to the beginning of stem elongation.

Acknowledgements

The authors gratefully acknowledge Josiane Jean-Jacques and Christelle Franchet for their excellent technical assistance. The PhD of Marion Gauthier was funded by a CIFRE convention between ITK and ANRT. The authors acknowledge ITK and Amélie Pinet for supporting the present work and for discussions.

References

Abichou M. 2016. Modélisation de l'architecture 4D du blé: identification des patterns dans la morphologie, la sénescence et le positionnement spatial des organes pour une large gamme de situations de croissance. PhD thesis, Université Paris-Saclay.

Albasha R, Fournier C, Pradal C, Chelle M, Prieto JA, Louarn G, Simonneau T, Lebon E. 2019. HydroShoot: a functional–structural plant model for simulating hydraulic structure, gas and energy exchange dynamics of complex plant canopies under water deficit—application to grapevine (*Vitis vinifera*). In Silico Plants **1**, diz007.

Andrieu B, Hillier J, Birch C. 2006. Onset of sheath extension and duration of lamina extension are major determinants of the response of maize lamina length to plant density. Annals of Botany **98**, 1005–1016.

Barillot R, Chambon C, Andrieu B. 2016a. CN-Wheat, a functional–structural model of carbon and nitrogen metabolism in wheat culms after anthesis. I. Model description. Annals of Botany **118**, 997–1013.

Barillot R, Chambon C, Andrieu B. 2016b. CN-Wheat, a functional–structural model of carbon and nitrogen metabolism in wheat culms after anthesis. II. Model evaluation. Annals of Botany **118**, 1015–1031.

Barillot R, Chambon C, Fournier C, Combes D, Pradal C, Andrieu B. 2019. Investigation of complex canopies with a functional–structural plant model as exemplified by leaf inclination effect on the functioning of pure and mixed stands of wheat during grain filling. Annals of Botany **123**, 727–742.

Barillot R, Escobar-Gutiérrez AJ, Fournier C, Huynh P, Combes D. 2014. Assessing the effects of architectural variations on light partitioning within virtual wheat–pea mixtures. Annals of Botany **114**, 725–737.

Begg JE, Wright MJ. 1962. Growth and development of leaves from intercalary meristems in phalaris arundinacea L. Nature **194**, 1097–1098.

Bertheloot J, Cournède PH, Andrieu B. 2011. NEMA, a functional-structural model of nitrogen economy within wheat culms after flowering. I. Model description. Annals of Botany **108**, 1085–1096.

Bertin N, Gary C. 1998. Short and long term fluctuations of the leaf mass per area of tomato plants—implications for growth models. Annals of Botany **82**, 71–81.

Boote KJ, Jones JW, White JW, Asseng S, Lizaso JI. 2013. Putting mechanisms into crop production models. Plant, Cell & Environment **36**, 1658–1672.

Brégard A, Allard G. 1999. Sink to source transition in developing leaf blades of tall fescue. New Phytologist **141**, 45–50.

Calderini DF, Dreccer MF, Slafer GA. 1997. Consequences of breeding on biomass, radiation interception and radiation-use efficiency in wheat. Field Crops Research **52**, 271–281.

Casey IA, Brereton AJ, Laidlaw AS, McGilloway DA. 1999. Effects of sheath tube length on leaf development in perennial ryegrass (*Lolium perenne* L.). Annals of Applied Biology **134**, 251–257.

Chelle M. 2005. Phylloclimate or the climate perceived by individual plant organs: what is it? How to model it? What for? New Phytologist **166**, 781–790.

Chelle M, Andrieu B. 1998. The nested radiosity model for the distribution of light within plant canopies. Ecological Modelling **111**, 75–91.

Coucheney E, Buis S, Launay M, *et al.* 2015. Accuracy, robustness and behavior of the STICS soil–crop model for plant, water and nitrogen outputs: evaluation over a wide range of agro-environmental conditions in France. Environmental Modelling & Software **64**, 177–190.

Coussement JR, De Swaef T, Lootens P, Roldán-Ruiz I, Steppe K. 2018. Introducing turgor-driven growth dynamics into functional-structural plant models. Annals of Botany **121**, 849–861.

Cutforth HW, Jame YW, Jefferson PG. 1992. Effect of temperature, vernalization and water stress on phyllochron and final main-stem leaf number of HY320 and Neepawa spring wheats. Canadian Journal of Plant Science **72**, 1141–1151.

Dale JE. 1985. The carbon relations of the developing leaf. In: Baker NR, Davies WJ, Ong CK, eds. Control of leaf growth. Cambridge: Cambridge University Press, 135–153.

DeJong TM, Da Silva D, Vos J, Escobar-Gutiérrez AJ. 2011. Using functional–structural plant models to study, understand and integrate plant development and ecophysiology. Annals of Botany **108**, 987–989.

Dornbusch T, Andrieu B. 2010. Lamina2Shape—An image processing tool for an explicit description of lamina shape tested on winter wheat (*Triticum aestivum* L.). Computers and Electronics in Agriculture **70**, 217–224.

Dornbusch T, Baccar R, Watt J, Hillier J, Bertheloot J, Fournier C, Andrieu B. 2011. Plasticity of winter wheat modulated by sowing date, plant population density and nitrogen fertilisation: dimensions and size of leaf blades, sheaths and internodes in relation to their position on a stem. Field Crops Research **121**, 116–124.

Dreccer MF, van Oijen M, Schapendonk AHCM, Pot CS, Rabbinge R. 2000. Dynamics of vertical leaf nitrogen distribution in a vegetative wheat canopy. Impact on canopy photosynthesis. Annals of Botany **86**, 821–831.

Durand JL, Schaufele R, Gastal F. 1998. Modelling the elongation of successive leaves on grass tillers. Effects of temperature, cutting height and cutting frequency. In: Zina M, Bartosova ML, eds. Short communications of the Vth Congress, European Society for Agronomy. Nitra, Slovakia, 28 June–2 July 1998, 141–142.

Durand J-L, Schäufele R, Gastal F. 1999. Grass leaf elongation rate as a function of developmental stage and temperature: morphological analysis and modelling. Annals of Botany **83**, 577–588.

Faverjon L, Escobar-Gutiérrez A, Litrico I, Julier B, Louarn G. 2019. A generic individual-based model can predict yield, nitrogen content, and species abundance in experimental grassland communities. Journal of Experimental Botany **70**, 2491–2504.

Fournier C, Andrieu B, Ljutovac S, Saint-Jean S. 2003. ADEL-wheat: a 3D architectural model of wheat development. In: Hu B-G, Jaeger M, eds. Proceedings PMA03: 2003 International symposium on plant growth modeling, simulation, visualization and their applications. Beijing: IEEE Computer Society, 54–63.

Fournier C, Andrieu B, Sohbi Y. 2001. Virtual plant models for studying interactions between crops and environment. In: Giambiasi N, Frydman C, eds. 13th European Simulation Symposium. Simulation in Industry. Marseilles, France, October 18–20, 2001. Proceedings. Erlangen: Society for Computer Simulation Europe Bvba, 476–480.

Fournier C, Durand JL, Ljutovac S, Schäufele R, Gastal F, Andrieu B. 2005. A functional–structural model of elongation of the grass leaf and its relationships with the phyllochron. New Phytologist **166**, 881–894.

Fournier C, Pradal C, Louarn G, Combes D, Soulié J-C, Luquet D, Boudon F, Chelle M. 2010. Building modular FSPM under OpenAlea: concepts and applications. In: Dejong TM, Da Silva D, eds. 6th International Workshop on Functional-Structural Plant Models. Davis, USA, September 12–17, 2010. Proceedings. Davis: University of California, 109–112.

Fricke W. 2002. Biophysical limitation of leaf cell elongation in source-reduced barley. Planta **215**, 327–338.

Friedli CN, Abiven S, Fossati D, Hund A. 2019. Modern wheat semi-dwarfs root deep on demand: response of rooting depth to drought in a set of Swiss era wheats covering 100 years of breeding. Euphytica **215**, 85.

Friend DJC, Helson VA, Fisher JE. 1965. Changes in the leaf area ratio during growth of marquis wheat, as affected by temperature and light intensity. Canadian Journal of Botany **43**, 15–28.

Garin G, Fournier C, Andrieu B, Houlès V, Robert C, Pradal C. 2014. A modelling framework to simulate foliar fungal epidemics using functional–structural plant models. Annals of Botany **114**, 795–812.

Gastal F, Nelson CJ. 1994. Nitrogen use within the growing leaf blade of tall fescue. Plant Physiology **105**, 191–197.

Gaudio N, Escobar-Gutiérrez AJ, Casadebaig P, *et al.* 2019. Current knowledge and future research opportunities for modeling annual crop mixtures. A review. Agronomy for Sustainable Development **39**, 20.

Godin C, Sinoquet H. 2005. Functional–structural plant modelling. New Phytologist **166**, 705–708.

Hammer G, Messina C, Wu A, Cooper M. 2019. Biological reality and parsimony in crop models—why we need both in crop improvement! In Silico Plants **1**, diz010.

Justes E, Mary B, Meynard J-M, Machet J-M, Thelier-Huché L. 1994. Determination of a critical nitrogen dilution curve for winter wheat crops. Annals of Botany **74**, 397–407.

Kätterer T, Hansson A-C, Andrén O. 1993. Wheat root biomass and nitrogen dynamics—effects of daily irrigation and fertilization. Plant and Soil **151**, 21–30.

Keith H, Oades JM, Martin JK. 1986. Input of carbon to soil from wheat plants. Soil Biology and Biochemistry **18**, 445–449.

Kemp DR. 1980. The growth rate of successive leaves of wheat plants in relation to sugar and protein concentrations in the extension zone. Journal of Experimental Botany **31**, 1399–1411.

Kemp DR. 1981. The growth rate of wheat leaves in relation to the extension zone sugar concentration manipulated by shading. Journal of Experimental Botany **32**, 141–150.

Ljutovac S. 2002. Coordination dans l'extension des organes aériens et conséquence pour les relations entre les dimensions finales des organes chez le blé. PhD thesis, Institut National Agronomique Paris-Grignon.

Lobet G, Pagès L, Draye X. 2014. A modeling approach to determine the importance of dynamic regulation of plant hydraulic conductivities on the water uptake dynamics in the soil-plant-atmosphere system. Ecological Modelling **290**, 65–75.

Longnecker N, Kirby EJM, Robson A. 1993. Leaf emergence, tiller growth, and apical development of nitrogen-dificient spring wheat. Crop Science **33**, 154–160.

Louarn G, Faverjon L. 2018. A generic individual-based model to simulate morphogenesis, C–N acquisition and population dynamics in contrasting forage legumes. Annals of Botany **121**, 875–896.

Lupton FGH, Oliver RH, Ellis FB, Barnes BT, Howse KR, Welbank PJ, Taylor PJ. 1974. Root and shoot growth of semi-dwarf and taller winter wheats. Annals of Applied Biology **77**, 129–144.

Luquet D, Dingkuhn M, Kim H, Tambour L, Clement-Vidal A. 2006. EcoMeristem, a model of morphogenesis and competition among sinks in rice. 1. Concept, validation and sensitivity analysis. Functional Plant Biology **33**, 309–323.

Malvoisin P. 1984. Organogenèse et croissance du maître-brin du blé tendre (*Triticum aestivum*) du semis à la floraison. II. - Contrôle des relations entre la croissance et la vascularisation de la tige et des feuilles. Essai de modélisation. Agronomie **4**, 587–596.

McMaster GS. 2005. Phytomers, phyllochrons, phenology and temperate cereal development. Journal of Agricultural Science **143**, 137–150.

Muller B, Martre P. 2019. Plant and crop simulation models: powerful tools to link physiology, genetics, and phenomics. Journal of Experimental Botany **70**, 2339–2344.

Parry MA, Reynolds M, Salvucci ME, Raines C, Andralojc PJ, Zhu XG, Price GD, Condon AG, Furbank RT. 2011. Raising yield potential of wheat. II. Increasing photosynthetic capacity and efficiency. Journal of Experimental Botany **62**, 453–467.

Poorter H, Anten NP, Marcelis LF. 2013. Physiological mechanisms in plant growth models: do we need a supra-cellular systems biology approach? Plant, Cell & Environment **36**, 1673–1690.

Poorter H, Niinemets U, Poorter L, Wright IJ, Villar R. 2009. Causes and consequences of variation in leaf mass per area (LMA): a meta-analysis. New Phytologist **182**, 565–588.

Pradal C, Dufour-Kowalski S, Boudon F, Fournier C, Godin C. 2008. OpenAlea: a visual programming and component-based software platform for plant modelling. Functional Plant Biology **35**, 751–760.

Pradal C, Fournier C, Valduriez P, Cohen-Boulakia S. 2015. OpenAlea: scientific workflows combining data analysis and simulation. In: SSDBM '15: Proceedings of the 27th International Conference on Scientific and Statistical Database Management. New York: Association for Computing Machinery, 11:1–11:6.

Prusinkiewicz P. 1998. Modeling of spatial structure and development of plants: a review. Scientia Horticulturae **74**, 113–149.

Rawson H, Gardner P, Long M. 1987. Sources of variation in specific leaf area in wheat grown at high temperature. Functional Plant Biology **14**, 287.

Reyes F, Pallas B, Pradal C, Vaggi F, Zanotelli D, Marco T, Gianelle D, Costes E. 2019. MuSCA: a multi-scale source-sink carbon allocation model to explore carbon allocation in plants. An application to static apple tree structures. Annals of Botany doi: 10.1093/aob/mcz122

Rogan PG, Smith DL. 1975. Rates of leaf initiation and leaf growth in *Agropyron repens* (L.) beauv. Journal of Experimental Botany **26**, 70–78.

Schnyder H, Nelson CJ. 1987. Growth rates and carbohydrate fluxes within the elongation zone of tall fescue leaf blades. Plant Physiology **85**, 548–553.

Schnyder H, Nelson CJ. 1989. Growth rates and assimilate partitioning in the elongation zone of tall fescue leaf blades at high and low irradiance. Plant Physiology **90**, 1201–1206.

Schnyder H, Schäufele R, Visser R de, Nelson CJ. 2000. An integrated view of C and N uses in leaf growth zones of defoliated grasses. In: Lemaire G, Hodgson J, de Moraes A, Nabinger C, Carvalho, PCF, eds. Grassland ecophysiology and grazing ecology. Wallingford: CABI Publishing, 41–60.

Siddiqi MY, Glass AD, Ruth TJ, Rufty TW. 1990. Studies of the uptake of nitrate in barley: I. kinetics of NO_3 influx. Plant Physiology **93**, 1426–1432.

Sievänen R, Godin C, DeJong TM, Nikinmaa E. 2014. Functional–structural plant models: a growing paradigm for plant studies. Annals of Botany **114**, 599–603.

Skinner RH, Nelson CJ. 1995. Elongation of the grass leaf and its relationship to the phyllochron. Crop Science **35**, 4–10.

Slattery RA, Ort DR. 2015. Photosynthetic energy conversion efficiency: setting a baseline for gauging future improvements in important food and biofuel crops. Plant Physiology **168**, 383–392.

Swinnen J, Van Veen JA, Merckx R. 1995. Carbon fluxes in the rhizosphere of winter wheat and spring barley with conventional vs integrated farming. Soil Biology and Biochemistry **27**, 811–820.

Tardieu F, Granier C, Muller B. 1999. Modelling leaf expansion in a fluctuating environment: are changes in specific leaf area a consequence of changes in expansion rate? New Phytologist **143**, 33–43.

Thornley JHM, Cannell MGR. 2000. Modelling the components of plant respiration: representation and realism. Annals of Botany **85**, 55–67.

Verdenal A, Combes D, Escobar-Gutiérrez AJ. 2008. A study of ryegrass architecture as a self-regulated system, using functional-structural plant modelling. Functional Plant Biology **35**, 911–924.

Vidal T, Andrieu B. 2019. Contrasting phenotypes emerging from stable rules: a model based on self-regulated control loops captures the dynamics of shoot extension in contrasting maize phenotypes. Annals of Botany doi: 10.1093/aob/mcz168

Volenec JJ, Nelson CJ. 1984. Carbohydrate metabolism in leaf meristems of tall fescue: II. Relationship to leaf elongation rates modified by nitrogen fertilization. Plant Physiology **74**, 595–600.

Vos J, Evers JB, Buck-Sorlin GH, Andrieu B, Chelle M, de Visser PH. 2010. Functional–structural plant modelling: a new versatile tool in crop science. Journal of Experimental Botany **61**, 2101–2115.

Williams RD. 1964. Assimilation and translocation in perennial grasses. Annals of Botany **28**, 419–426.

Williams RF. 1975. Shoot apex and leaf growth. Cambridge: Cambridge University Press.

Williams RF, Rijven AHGC. 1965. The physiology of growth in the wheat plant. II. The dynamics of leaf growth. Australian Journal of Biological Sciences **18**, 721–743.

Williams RF, Williams CN. 1968. Physiology of growth in the wheat plant IV. Effects of day length and light energy level. Australian Journal of Biological Sciences **21**, 835–854.

Zhao Z, Wang E, Wang Z, Zang H, Liu Y, Angus JF. 2014. A reappraisal of the critical nitrogen concentration of wheat and its implications on crop modeling. Field Crops Research **164**, 65–73.

Zhu J, Andrieu B, Vos J, van der Werf W, Fournier C, Evers JB. 2014. Towards modelling the flexible timing of shoot development: simulation of maize organogenesis based on coordination within and between phytomers. Annals of Botany **114**, 753–762.